LPTN-Based Real-Time Stator Hotspot Temperature Estimation for Enhanced Thermal Management in High-Performance PMSMs

IEEE Access
Multidisciplinary | Rapid Review | Open Access Journal

RESEARCH ARTICLE

LPTN-Based Real-Time Stator Hotspot Temperature Estimation for Enhanced Thermal Management in High-Performance PMSMs

PAOLO PESCETTO, (Member, IEEE), GAETANO DILEVRANO, GIANMARIO PELLEGRINO, (Fellow, IEEE), AND ALDO BOGLIETTI, (Fellow, IEEE)
Department of Energy "Galileo Ferraris," Politecnico di Torino, 10129 Turin, Italy
Corresponding author: Paolo Pescetto (paolo.pescetto@polito.it)

ABSTRACT Thermal management is critical for high-performance electric motor drives with compact design and extreme overload capability, resulting in significant temperature gradients within the stator winding. Due to limited access to the winding hotspot, conventional temperature sensors cannot directly measure the peak hotspot temperature, which can fluctuate rapidly during operation and often exceeds accessible measurements. This constraint requires high thermal safety margins, limiting, in practice, the motor's peak torque potential. This work deals with hotspot temperature monitoring and prediction for synchronous motor drives. This paper presents a real-time hotspot temperature monitoring solution using an advanced Lumped Parameter Thermal Network (LPTN) model. The proposed LPTN is analytically solvable, enabling efficient implementation on automotive-grade microcontrollers. Parameters are calibrated through simple experimental tests, eliminating the need for detailed motor geometry knowledge. Experimental validation on a high-performance traction PMSM under real driving conditions shows that the model achieves a residual estimation error of approximately 5° C, demonstrating reliable tracking of the winding hotspot during severe thermal transients.

INDEX TERMS Electric motors, thermal model, short-time thermal transient, hotspot temperature estimation, stator winding, temperature observer, real-time temperature tracking.

NOMENCLATURE

C_w, C_{Fe}	Thermal capacitance of stator winding and iron.
C_m, C_h	Thermal capacitance of the two winding portions m and h.
θ, θ_m, θ_h	Average winding temperature and temperatures of the measurable and hotspot points.
P_j, P_{Fe}	Total Joule loss and iron loss.
P_{jm}, P_{jh}	Joule loss of the two winding parts m and h.
R_{eq}	Equivalent thermal resistance between stator winding and iron.
R_{mf}, R_{hf}, R_{mh}	Thermal resistance between the winding portion m and the stator iron, between the portion h and the iron, and between m and h portions (delta connected).
R_m, R_h, R_f	Equivalent star resistances of R_{mf}, R_{hf}, R_{mh}.
R_{fa}	Thermal resistance between iron and ambient.
R_{ff}	Series of R_f and R_{fa}.
x, y	Ratio C_h/C_w and R_f/R_{ff}.

I. INTRODUCTION

High performance applications of electrical motor drives such as traction and robotics are constantly pushing for increased torque and power density [1], [2], [3]. This requires targeting volume and weight reduction while increasing the current density. This increases the associated Joule losses,

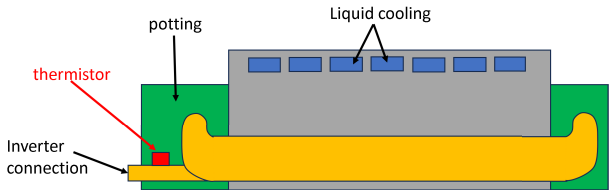

FIGURE 1. Schematic of the motor structure.

while reducing the surface available for heat dissipation. In this scenario, advanced cooling systems play a crucial role in the design and safe operation of the drive.

Highly loaded e-motors shows extremely uneven temperature distributions [4]. The stator winding is one of the most critical components and its hotspot temperature must be limited to avoid faults and premature aging of the insulation [5], [6], [7]. Most traction motors embed one or more winding thermistors, but unfortunately, the hottest point is rarely accessible in highly compact machines [8], impeding its direct temperature measurement during operation. For example, as can be seen in Fig. 1, the Motor Under Test (MUT) has a single thermistor in the only accessible winding point, i.e. close to the phases connection with the inverter, which is considerably colder than hotspot, located in more internal parts of the machine. Moreover, the hotspot temperature and the temperature measured by the thermistor have different dynamics during the drive operation, so the temperature difference depends on the driving cycle, adding a further source of uncertainty. In light of this behavior, the hotspot temperature remains largely unknown, and a large safety margin is required when defining the motor current and torque limits, to avoid temperature-related failures.

Several real-time temperature observers were proposed in the literature, including the monitoring of the inverter [9], PM [10] and winding temperature [11], [12], [13]. Focusing on stator winding temperature observers, these are normally based on the estimation of the stator resistance variation [13], or the dynamic inductance [12]. However, techniques like [11], [12], [13] can only estimate the average winding temperature, which is often far from the hotspot value in highly loaded cases.

Thermal models can be classified into two main categories [14], i.e. based on Finite Element Analysis (FEA) or on Lumped Parameters Thermal Networks (LPTN). FEA thermal models [15], [16] provide a detailed representation of the temperature distribution inside the machine, but cannot be executed in real-time by the microcontrollers. Moreover, a proper representation of thermal transients is sensitive to the model's parameters, requiring a fine calibration of the materials' properties, which are hardly measured in experiments. On the other hand, the LPTN approach coarsely simplifies the machine using a reduced number of temperature nodes [17], modeling each sub-body of the motor in terms of thermal capacitances, and the heat flow between bodies through equivalent thermal resistances. This is at risk of oversimplification, but with extremely lower computational effort. Oversimplified models such as [18] represent the stator winding as a single node at a uniform temperature, thus not monitoring its hotspot. This approach is unfeasible for the considered application due to the high thermal gradient and the fast dynamics of the hotspot temperature. A more sophisticated approach is proposed in [17], [19], and [20], using more complicated, higher-order networks, which are difficult to calibrate and hardly compatible with real-time execution within the motor control routine. Moreover, previous papers like [17], [18], [19], [20] deal with relatively slow thermal transients with time constants in the order of 10 to 30 minutes, while a much higher dynamics was observed in the application under test.

A major drawback of most of the LPTNs in the literature is that their parameters are not identified through a dedicated experimental session. The thermal parameters are often computed based on design-level data such as the machine geometry and the materials' properties [4], [17] (open-loop approach), which are hardly available to the end user. Moreover, the effects of the manufacturing process (e.g. potting) on thermal dissipation are hardly evaluated, as well as parametric dispersion between machines of the same series. A second possibility to identify the LPTN parameters is to train the network based on thermal cycles [20], [21] (data-driven approach), e.g. by numerically searching the set of parameters that minimizes the error in temperature prediction. This requires a high number of training load cycles, and it might lead to a nonphysical representation of the machine, with non-reasonable thermal resistances or capacitances, especially in the case of a high number of thermal nodes. Moreover, the optimization algorithm starts from a tentative LPTN calibration, which again requires good knowledge of the motor design.

This work proposes a novel real-time observer based on an advanced LPTN. The main advantages with respect to existing techniques [4], [17], [18], [19], [20], [21], [22] are:

- The observer is capable of dynamically estimating the temperature of the hottest point of the stator winding during the drive operation. This allows for fully exploiting the transient overload capability of the drive while ensuring its reliability against thermal failure.
- The LPTN is analytically solved and designed in the discrete-time domain, thus enabling its direct implementation on any up-to-date microcontroller.
- A dedicated experimental procedure is proposed, permitting the direct determination of all the parameters of the hot-spot observer through simple DC characterization tests, ensuring good accuracy and reliability of the calibration without requiring prior knowledge of the geometry or thermal properties of the winding.
- The thermal commissioning tests and the related data processing are extensively described, to permit the automatic calibration of the observer;

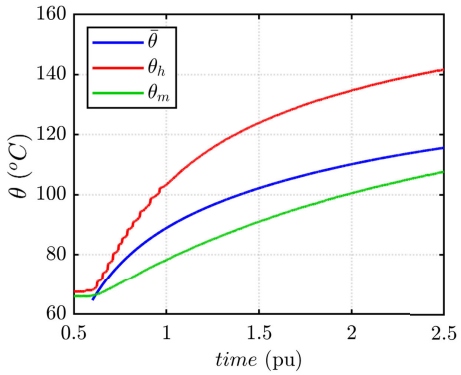

FIGURE 2. Example of simulated transient on the MUT. average (blue), hotspot (red) and measured (green) temperatures.

- The observer is fully validated on a commercial high-performance traction motor through both FEA simulations and experimental tests, demonstrating good performance under extremely fast temperature transients. The experiments were conducted both on a dedicated test bench and with the motor mounted on the target vehicle, emulating real driving cycle conditions.
- A sensitivity analysis of the estimated hotspot temperature over the observer calibration proves its high robustness against inaccurate loss determination.
- The scalability of the proposed approach is demonstrated by testing a second high performance traction motor with considerably larger torque ratings.

II. MOTOR UNDER TEST

The MUT is a Permanent-Magnet Synchronous Motor (PMSM) for traction applications, designed for high-performance hypercars. The stator is liquid-cooled, as reported in Fig. 1. The nominal power of the machine is higher than 100 kW, with a maximum speed higher than 20 krpm. The detailed motor geometry and materials are covered by the industrial property of the carmaker and cannot be disclosed. For the same reason, every physical quantity is reported as normalized per unit (pu).

A. MOTOR MODEL AND FEA SIMULATIONS

At first, the location of the winding hotspot was evaluated, considering both longitudinal and radial thermal gradients. A thermal analysis of the motor was conducted [23], with an accurate model developed by the carmaker. The simulations were conducted under different speeds and loads, including standard and custom driving cycles. This permitted to identify the position of the most critical winding hotspot, which resulted up to 90° C hotter than the measurable point.

In particular, the MUT was simulated both through 2D thermal FEAs, focusing on the motor section, and a 3D LPTN. This LPTN presents a high number of nodes, permitting a precise representation of the radial and longitudinal thermal gradients, with the thermal resistances and capacitances of the network defined by the motor geometry and materials. In addition to the active length of the machine, the model also incorporates the winding ends and inverter connections. To account for the radial thermal gradient, the winding is divided into multiple layers, distinguishing between the inner and outer conductors, which experience different thermal conditions. Moreover, the model includes winding potting and stator liquid cooling. It was calibrated directly by the carmaker, drawing on their expertise and experimental validation from similar motors.

An example of a simulated thermal transient is given in Fig. 2, where a load step was applied starting with the motor at room temperature. The picture reports the average winding temperature $\bar{\theta}$, and the temperatures of the hotspot θ_h and measurable θ_m points. Despite this not being the worst case scenario, it can be observed that the hotspot temperature sharply rises, while the measurable point follows with a remarkably slower dynamic. The temperature gradient is even more significant under complex load cycles. This confirms the necessity of a real-time estimator capable of tracking the winding hotspot temperature in transient conditions.

B. PROTOTYPE MANUFACTURING AND CHARACTERIZATION

After the simulation campaign, a prototype was manufactured. Seven thermistors permit experimentally mapping its thermal gradient, including the hotspot. In the embarkable version, the insertion of such additional thermistors is unfeasible, as it would compromise the mechanical integrity of the stator and its resilience to NVH. Therefore, the embarkable version embeds only one thermistor in an accessible point of the winding close to the phases connection with the inverter, as depicted in Fig. 1. Since this point is thermally distant from the center of the machine, the measured temperature is lower than the average and hotspot temperatures, in accordance with the transient depicted in Fig. 2.

The prototype was thermally characterized in experiments, following the method in [24] and [25]. The thermal characterization included a Short-Time Thermal Transient (STTT) test [25] and a Steady State (SS) test. In both cases, the motor is excited with a DC power supply, but if the STTT focuses on the initial part of the thermal transient, the SS test detects the regime measured, average and hotspot temperatures.

1) SHORT TIME THERMAL TRANSIENT TEST

The STTT is a testing procedure originally developed for industrial motors [26], and then extended to the more complicated case of high performance drives [25], hardly covered by the standard tests [27]. This includes traction applications, with high torque density, advanced cooling systems and high-rate heat exchange. The advanced

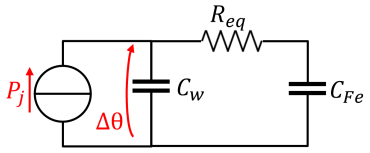

FIGURE 3. Equivalent LPTN for the improved STTT test.

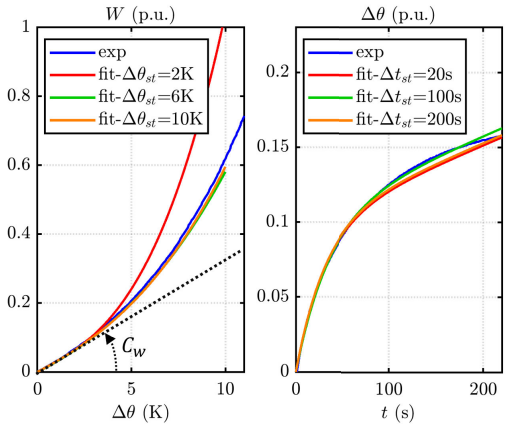

FIGURE 4. Results of the STTT [25]: measured energy $W(\Delta\theta)$ and temperature rise $\Delta\theta(t)$ interpolated on varying $\Delta\theta_{st}$ and Δt_{st} respectively.

STTT in [25] determines the winding and iron thermal capacitances C_w and C_{Fe} and an equivalent winding-to-iron thermal resistance, called R_{eq}.

The three phases are connected in series, to ensure a homogeneous heating of the machine. If the output terminals of the three phases are not available, so the three phases cannot be series connected, [25] proposes an alternative testing configuration, equivalent to the series excitation. Starting with the motor at uniform temperature θ_0, a DC power supply imposes a current compatible with the nominal motor current to the series of the three phases, thus producing a measurable temperature rise. The DC current i_{dc} and voltage v_{dc} are measured, thus monitoring the DC resistance R_{dc} and the corresponding Joule loss P_j. The average winding temperature is estimated from the resistance variation:

$$\theta = \frac{R_{dc}}{R_0}(234.5 + \theta_0) - 234.5 \tag{1}$$

where R_0 is the winding resistance at θ_0. Due to the DC series excitation, the injected power entirely converts into Joule loss, which is integrated to get the dissipated energy:

$$W = \int_{t_0}^{t} v_{dc} \cdot i_{dc}\, dt \tag{2}$$

where t_0 is the start of DC excitation, associated with zero energy loss. As said, the STTT focuses on the initial thermal transient, i.e. on the time interval called Δt_{st} [25], in the order of a few minutes. During this initial DC transient, the motor is interpreted with the second order LPTN in Fig. 3. The energy function of the temperature rise is approximated with a third-order Taylor series expansion, considering the temperature domain [0 $\Delta\theta_{st}$], and its initial derivative provides the winding thermal capacitance C_w:

$$\hat{W}(\Delta\theta) = a_3 \cdot \Delta\theta^3 + a_2 \cdot \Delta\theta^2 + a_1 \cdot \Delta\theta \tag{3}$$

$$\left.\frac{d\hat{W}}{d\Delta\theta}\right|_{\Delta\theta=0} = a_1 \quad \rightarrow \quad C_w = a_1 \tag{4}$$

The measured temperature rise is fitted by the analytical solution of the network in Fig. 3:

$$\hat{\Delta\theta}(t) = \frac{P_j}{C_w + C_{Fe}} t + P_j R_{eq} \frac{C_{Fe}^2}{(C_w + C_{Fe})^2}\left(1 - e^{-t/\tau_{eq}}\right) \tag{5}$$

$$\tau_{eq} = \frac{C_w C_{Fe}}{C_w + C_{Fe}} \cdot R_{eq} \approx C_w \cdot R_{eq} \tag{6}$$

The fitting results provide the iron capacitance C_{Fe} and the equivalent resistance R_{eq}. More details can be found in [25], where the same motor prototype was adopted. The plots reported in Fig. 4 show the measured energy and temperature rise (in blue) fitted considering different over temperature $\Delta\theta_{st}$ and time Δt_{st} domains.

It should be noted that the STTT focuses on the slot thermal model, i.e. the winding thermal capacitance and the thermal resistance between winding and stator iron, while the thermal coupling with the cooling system is not effective in the considered time horizon $t < \Delta t_{st}$. For this reason, the STTT does not imposes any constraints to the temperature and flow rate of the cooling system, which can eventually be disabled during the test.

2) DC STEADY STATE TEST

The SS test requires the same excitation and measurement setup used for the STTT. If the STTT focuses on the first few minutes of DC excitation, the SS test measures the winding temperature when the thermal regime is reached. Again, the excitation voltage v_{dc} and current i_{dc} are monitored. The DC excitation permits to accurately evaluate the regime power loss $P_{j,dc}$, without any influence from the AC or iron losses. The steady-state over temperatures of the measurable and the hotspot points are called $\Delta\theta_m^{ss}$ and $\Delta\theta_h^{ss}$ respectively, and permit to compute the equivalent steady-state thermal resistances R_m^{ss} and R_h^{ss}:

$$\begin{cases} R_m^{ss} = \dfrac{\Delta\theta_m^{ss}}{P_{j,dc}} = \left.\dfrac{\Delta\theta_m}{v_{dc} \cdot i_{dc}}\right|_{t\to\infty} \\ R_h^{ss} = \dfrac{\Delta\theta_h^{ss}}{P_{j,dc}} = \left.\dfrac{\Delta\theta_h}{v_{dc} \cdot i_{dc}}\right|_{t\to\infty} \end{cases} \tag{7}$$

The SS test focuses on the thermal coupling with the cooling system. The test results are analyzed in terms of temperature rise relative to θ_a, which equals the coolant temperature. Consequently, the extracted thermal parameters do not depend on θ_a. However, the resistances measured

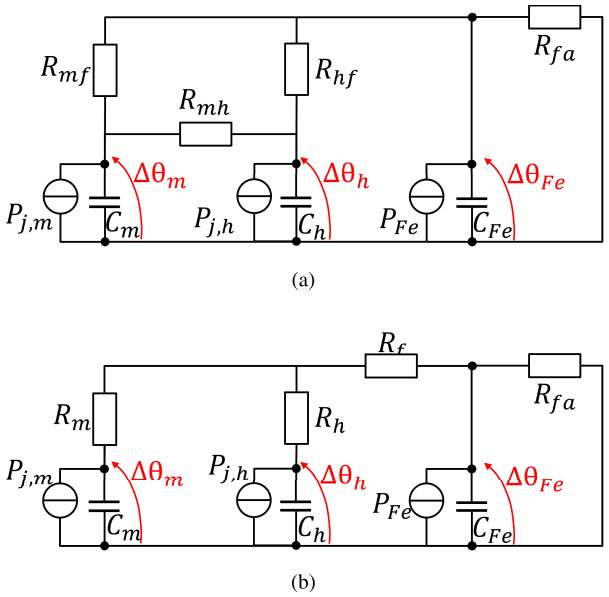

FIGURE 5. LPTNs proposed for hotspot temperature estimation. (a) Physical model, delta connected. (b) Star connected model, for calibration purposes and real-time execution.

in (7) are influenced by the coolant flow rate, which must be maintained at its nominal value during the SS test.

III. PROPOSED HOTSPOT TEMPERATURE OBSERVER

A. STATOR AND ROTOR DECOUPLING

The focus of this work is on tracking the winding temperature hotspot. The motor temperature is influenced by the stator and rotor losses, while the heat is dissipated mostly through the liquid cooling, and partially through the rotor, shaft, end winding and so on. Otherwise said, the stator and the rotor are thermally coupled. Nevertheless, the stator-to-rotor thermal time constant is considerably slower than the thermal coupling between the measurable and hotspot winding points. A temperature rise in the rotor produces an increase of both the measurable and hotspot temperatures, with negligible difference in terms of dynamic. This was verified both by FEA and experimental evidence, and it is mainly due to the airgap, which introduces a relevant thermal barrier to the heat transfer between stator and rotor. Therefore, the rotor losses and thermal dynamics can be disregarded when designing a stator hotspot observer, provided that a thermistor is present in the accessible winding point. For this reason, the proposed hotspot observer only models the stator behavior, neglecting the rotor losses and temperature dynamics.

In any case, if a rotor thermal model is available this can be added to the proposed stator LPTN, described in the next Section, further refining the hotspot temperature estimation.

B. STATOR LPTN

In the proposed LPTN for hotspot temperature observer is shown in Fig. 5a. Despite the continuous temperature variation within the winding, the observer was designed by discretizing the winding into two sections with uniform temperature: sector h, which contains the hotspot, and sector m, which includes the inverter connection where the thermistor is located (see Fig. 1). This discretization approach enables simple real-time execution, compatible with automotive-grade microcontrollers, while effectively distinguishing between the unknown hotspot temperature θ_h and the measurable temperature θ_m.

A thermal capacitance is associated with each winding section (C_m and C_h respectively), as well as the corresponding Joule loss P_{jm}, P_{jh}. Both the capacitance and the losses are assumed proportional to the volume of the corresponding winding section. The aggregate of C_m and C_h constitutes the total winding thermal capacitance C_w:

$$\begin{cases} C_h &= x \cdot C_w \\ C_m &= (1-x) \cdot C_w \end{cases} \tag{8}$$

$$0 < x < 1 \tag{9}$$

being x the fraction of the winding associated with the hotspot. Similarly, for copper losses:

$$\begin{cases} P_{jh} &= x \cdot P_j \\ P_{jm} &= (1-x) \cdot P_j \end{cases} \tag{10}$$

where P_j aggregates the stator AC and DC copper losses.

The stator iron thermal capacitance C_{Fe}, temperature θ_{Fe} and losses P_{Fe} are also introduced. Dealing with heat transfer, the thermal resistances R_{mf} and R_{hf} model the thermal coupling between each winding section and the stator iron, R_{mh} the interaction between the two winding sections and R_{fa} is the iron-to-ambient thermal resistance. In order to maintain a low complexity of the LPTN, the direct heat dissipation from the winding to the ambient (e.g. through end-windings) is reasonably neglected.

The system is described in terms of overtemperature with respect to the ambient temperature θ_a:

$$\begin{cases} \Delta\theta_h &= \theta_h - \theta_a \\ \Delta\theta_m &= \theta_m - \theta_a \\ \Delta\theta_{Fe} &= \theta_{Fe} - \theta_a \end{cases} \tag{11}$$

Since the motor under test is a liquid-cooled PMSM, θ_a is assumed to be equal to the inlet liquid temperature, a value typically measured in traction drives. The resulting LPTN, depicted in Fig. 5a. A $\Delta - Y$ transformation can be applied to the three resistances R_{mf}, R_{hf} and R_{mh}, leading to the LPTN reported in Fig. 5b:

$$\begin{cases} R_m = \dfrac{R_{mf} \cdot R_{mh}}{R_{mf} + R_{mh} + R_{hf}} \\ R_h = \dfrac{R_{hf} \cdot R_{mh}}{R_{mf} + R_{mh} + R_{hf}} \\ R_f = \dfrac{R_{mf} \cdot R_{hf}}{R_{mf} + R_{mh} + R_{hf}} \end{cases} \tag{12}$$

It is worth mentioning that the two LPTNs in Fig.s 5a and 5b are analytically equivalent, but if the first one

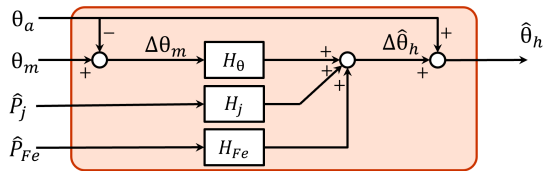

FIGURE 6. Block diagram of the MISO hotspot temperature observer.

is a realistic thermal network, the second one permits a more simple solution, calibration and real-time implementation. So, this latter LPTN will be considered in the following Sections.

IV. OBSERVER DESIGN AND CALIBRATION

The proposed temperature observer is a Multiple Input Single Output (MISO) system, reported in Fig. 6. It presents three inputs, i.e. the measured overtemperature $\Delta\theta_m$ and the estimated Joule and iron losses $\hat{P}_j$, $\hat{P}_{Fe}$, and a single output, i.e. the observed hotspot overtemperature $\Delta\theta_h$.

In the working range of the drive, e.g. between 0° C and 200° C, the thermal properties of all the material in the stator (copper, iron, isolation, potting, ...) do not significantly vary. For this reason, the system is considered linear, and the effects superposition holds.

A. LPTN SOLUTION

The LPTN in Fig. 5b is solved in the Laplace domain:

$$\hat{\Delta\theta}_h = \left.\frac{\hat{\Delta\theta}_h}{\Delta\theta_m}\right|_{\Delta\theta_m} \cdot \Delta\theta_m + \left.\frac{\hat{\Delta\theta}_h}{P_j}\right|_{P_j} \cdot \hat{P}_j + \left.\frac{\hat{\Delta\theta}_h}{P_{Fe}}\right|_{P_{Fe}} \cdot \hat{P}_{Fe} \tag{13}$$

$$\hat{\Delta\theta}_h = H_\theta \cdot \Delta\theta_m + H_j \cdot \hat{P}_j + H_{Fe} \cdot \hat{P}_{Fe} \tag{14}$$

The three transfer functions H_θ, H_j and H_{Fe} can be combined, and explicated as:

$$\hat{\Delta\theta}_h(s) = \frac{(a_\theta s + b_\theta)\,\Delta\theta_m + (a_j s + b_j)\,\hat{P}_j + b_f \hat{P}_{Fe}}{p_1 s^2 + p_2 s + p_3} \tag{15}$$

The three transfer functions $H_\theta(s)$, $H_j(s)$ and $H_{Fe}(s)$ share the same two poles, corresponding to the poles of the physical system. The LPTN solution (15) presents seven parameters, that can be analytically determined from the four thermal resistances and three capacitances:

$$\begin{cases} a_\theta = R_{fa} R_f C_{Fe} \\ b_\theta = R_{fa} + R_f \\ a_j = R_{fa}\left(R_f R_m + R_f R_h + R_m R_h\right) C_{Fe} \\ b_j = R_f R_m + R_f R_h + R_m R_h + R_m R_{fa} + R_h R_{fa} \\ b_f = R_m R_f a \\ p_1 = C_{Fe} C_h R_{fa}\left(R_h R_f + R_m R_f + R_h R_m\right) \\ p_2 = C_{Fe} R_{fa}\left(R_f + R_m\right) + \\ \quad + C_h\left(R_h R_f + R_m R_f + R_h R_m + R_h R_{fa} + R_m R_{fa}\right) \\ p_3 = R_f + R_m + R_{fa} \end{cases} \tag{16}$$

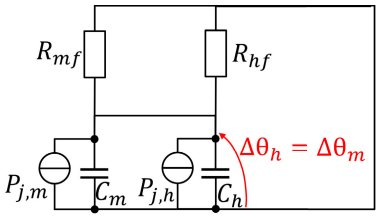

FIGURE 7. Equivalent LPTN for the STTT test.

The analytical derivation of (16) is omitted for brevity, but can be easily obtained by solving the LPTN in Fig. 5b. Notably, the coolant temperature θ_a is incorporated into the LPTN solution, which is expressed in terms of overtemperatures (11). As a result, the hotspot temperature can be estimated independently of the inlet coolant temperature.

B. DISCRETE-TIME IMPLEMENTATION

The hotspot observer can be implemented as in Fig. 6, and embedded in a real-time control. For this purpose, each transfer function appearing in (14), i.e. $H_\theta(s)$, $H_j(s)$ and $H_{Fe}(s)$ are discretized. Taking as an example $H_\theta(s)$, this can be discretized as $H_\theta(z)$:

$$H_\theta(z) = \frac{-\frac{a_\theta}{T_s} z^{-1} + \left(\frac{a_\theta}{T_s} + b_\theta\right)}{\frac{p_1}{T_s^2} z^{-2} - \left(\frac{2p_1}{T_s^2} z^{-2} + \frac{p_2}{T_s}\right) z^{-1} + \left(\frac{p_1}{T_s^2} z^{-2} + \frac{p_2}{T_s} + !p_3\right)} \tag{17}$$

where T_s is the sampling time. The discretized form of the two transfer functions $H_j(z)$ and $H_{Fe}(z)$ is not reported for brevity, but they are in the same form of (17). Once translated into c-code, this transfer function requires only a small number of multiplications and additions, resulting in a negligible computational overhead for automotive-grade microcontrollers.

It should be noted that the thermal time constants are in the order of magnitude of 5÷500 s, i.e. considerably slow with respect to the typical sampling frequency of the real-time controller (tens of kHz). So, the discretization error in $H_\theta(z)$, $H_j(z)$ and $H_{Fe}(z)$ is minimal and it does not introduces any significant effect on the hotspot temperature prediction.

C. HOTSPOT OBSERVER CALIBRATION

One of the key issues with most of the temperature observers is the determination of the LPTN parameters, i.e. the four thermal resistances and three capacitances. These could be determined based on the motor geometry and materials, but this information is often uncertain due to the complex geometry of the design and to the manufacturing tolerance. Therefore, an experimental-based calibration procedure is strongly preferred, measuring the LPTN parameters directly on the MUT. In this work, the proposed calibration procedure is based on the two characterization tests

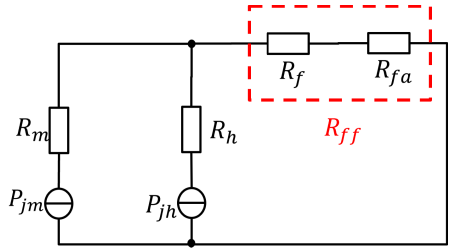

FIGURE 8. Equivalent LPTN for the DC steady state test.

described in Section II, i.e. the STTT and the SS tests. The STTT estimates C_w, C_{Fe} and R_{eq}, while the SS test provides R_m^{ss} and R_h^{ss}. A dedicated post-processing is proposed to extract the LPTN parameters from the results of the two tests.

In particular, the winding capacitance measured through the STTT permits computing the capacitances C_h and C_m according to (8), where the coefficient x is arbitrarily imposed. Moreover, during the STTT, i.e. on the initial part of the thermal transient, the following hypotheses can be assumed:

- the iron losses are null due to DC excitation of the STTT, and the stator iron remains at room temperature ($\Delta\theta_{Fe} = 0$, $P_{Fe} = 0$);
- the temperature of the two parts of the winding grows simultaneously, i.e. the winding temperature can be considered uniform ($\Delta\theta_h = \Delta\theta_m$)

The second hypothesis corresponds to shorting the resistance R_{mh}. Therefore, the two winding sections can be aggregated, leading to the equivalent LPTN in Fig. 7. By comparing this network with the one in Fig. 4, i.e. the equivalent LPTN valid for the STTT, the aggregate thermal resistance R_{eq} estimated by the STTT can be interpreted as:

$$R_{eq} = R_{mf} \parallel R_{hf} = R_f \tag{18}$$

Otherwise said, the thermal resistance R_{eq} measured in the STTT test can be interpreted as the thermal resistance R_f.

Dealing with the SS test, at DC thermal regime the LPTN in Fig. 5b is simplified as in Fig. 8, where all the capacitances and the iron loss term were removed. The series of the thermal resistances R_f and R_{fa} is called R_{ff}.

$$R_{ff} = R_f + R_{fa} \tag{19}$$

Moroever, the parameter y is introduced:

$$y = \frac{R_f}{R_{ff}} \tag{20}$$

The steady state solution of this DC network, again written in terms of overtemperatures, is:

$$\begin{cases} \Delta\theta_m^{ss} = P_j R_{ff} + (1-x) P_j R_m \\ \Delta\theta_h^{ss} = P_j R_{ff} + x P_j R_h \end{cases} \tag{21}$$

The same solution can be written in terms of SS equivalent thermal resistances:

$$\begin{cases} R_m^{ss} = R_{ff} + (1-x) R_m \\ R_h^{ss} = R_{ff} + x R_h \end{cases} \tag{22}$$

By manipulating (18) and (22), all the resistances of the LPTN can be evaluated and expressed as a function of the commissioning measures and the x and y coefficients:

$$\begin{cases} R_m = \dfrac{R_m^{ss} - \dfrac{R_{eq}}{y}}{(1-x)} \\ R_h = \dfrac{R_h^{ss} - \dfrac{R_{eq}}{y}}{x} \\ R_f = R_{eq} \\ R_{fa} = R_{eq} \cdot \dfrac{1-y}{y} \end{cases} \tag{23}$$

Finally, to guarantee a physical meaning of the LPTN parameters, i.e. imposing all the thermal capacitances and resistances being greater than zero, and considering $R_h^{ss} > R_m^{ss}$, the parameter y is bounded as follows:

$$\frac{R_{eq}}{R_m^{ss}} < y < 1 \tag{24}$$

Overall, the LPTN parameters are fully calibrated based on the STTT and SS tests and two arbitrary parameters x and y, which are the only two coefficients determined based on the user's experience. Nevertheless, x and y are bounded in a narrow range (9), (24), simplifying the tuning procedure. Once the coefficients are determined, the hotspot temperature observer is implemented according to Fig. 6, discretized based on (17) and embedded in the motor control algorithm, for real-time $\hat{\theta}_h$ monitoring during the drive operation.

V. SIMULATION AND EXPERIMENTAL RESULTS

The proposed hotspot temperature observer was validated:

- in simulation, using an accurate model provided by the carmaker on a commercial solver [23];
- in experiments in a dedicated e-axle test bench (Fig. 9a);
- in experiments with the drive mounted on the target application, in a vehicle test bench.

Both the e-axle and the vehicle test benches can emulate real driving cycles. In all the reported tests, the coolant temperature and flow rate were imposed to their nominal values, according to the motor manufacturer's specifications. For the e-axle bench only, the motor voltage, current, and torque are monitored with an HBK Gen7t data recorder, depicted in Fig. 9b. The vehicle test bench is not depicted due to confidentiality issues. If the commercial motor only embeds one thermistor in the only accessible point of the machine, the prototype presents six additional thermistors, including the hotspot. A DAT4135 board, shown in Fig. 9c, is adopted for conditioning the temperature measurement.

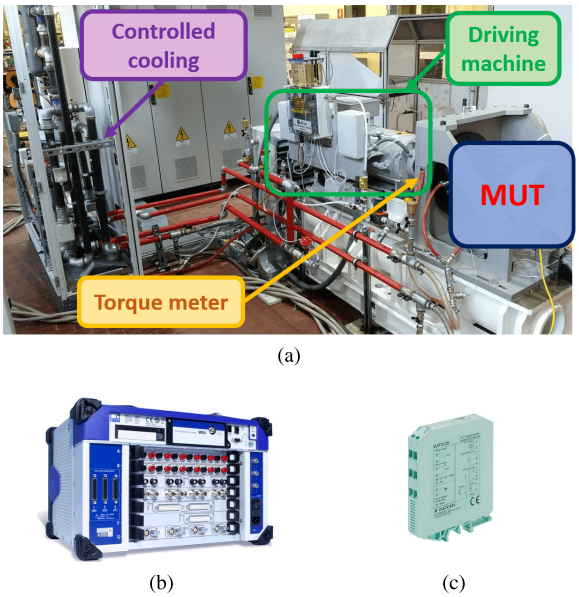

FIGURE 9. a) e-Axle test bench adopted for experimental validation. b) HBK Gen7t data recorder and c) DAT4135 for the conditioning of temperature measurement adopted in the e-axle test bed.

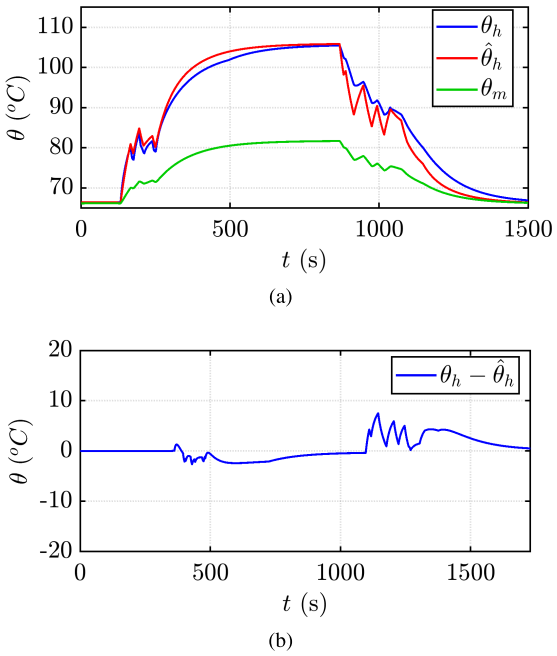

FIGURE 10. Simulated temperature prediction under DC motor excitation. a) Blue and red: measured and estimated hotspot temperature; green: accessible measurement point. b) Temperature estimation error.

A. INVESTIGATION OF JOULE LOSS EFFECT

As a first validation, executed both in simulation and in the e-axle test bed, the motor was tested at standstill. A reference load profile was considered composed of a sequence of torque steps, covering short-time overload, idles, and longer periods at partial load. Based on this cycle, the corresponding P_j were computed and imposed through a DC excitation of the MUT. Otherwise said, the amplitude of the DC current was computed to obtain the losses expected from

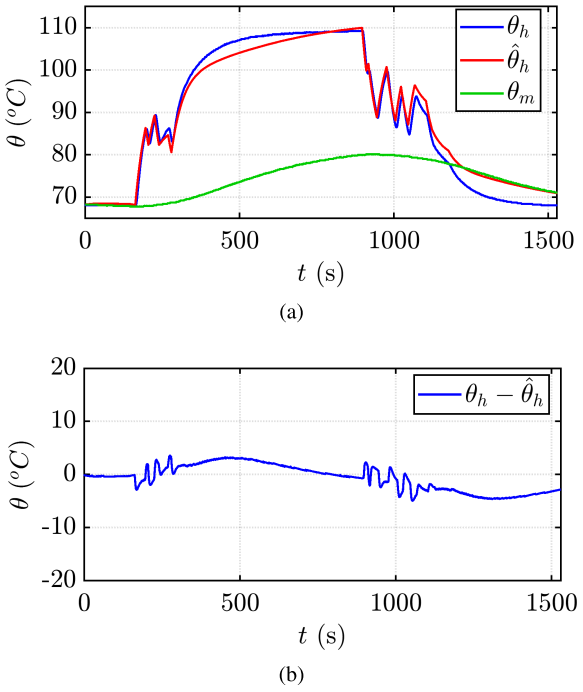

FIGURE 11. e-Axle test: temperature prediction under DC motor excitation. a) Blue and red: measured and estimated hotspot temperature; green: accessible measurement point. b) Temperature estimation error.

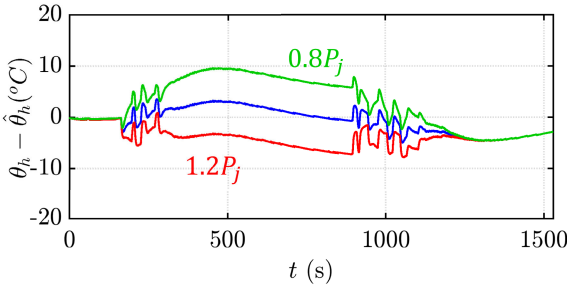

FIGURE 12. e-Axle test: sensitivity of temperature estimation error under DC motor excitation and uncertain $\hat{P}_j$. Blue: accurate $\hat{P}_j$; red: $\hat{P}_j$ overestimated by 20%; green: $\hat{P}_j$ underestimated by 20%.

the reference load cycle. This DC excitation permitted to investigate the effect of P_j on the temperature distribution while eliminating the effects of iron losses. The hotspot temperature is given by (15) with $\hat{P}_j$ easily computed from the DC voltage and current, while $P_{Fe} = 0$. The results are reported in Fig.s 10 and 11 for the simulated and experimental test respectively. Both cases clearly show the difference between the measurable (green line) and hotspot (blue line) temperatures, confirming a significant thermal gradient. Moreover, both in simulation and experiments, the hotspot temperature dynamic is considerably faster then the measurable point. Still, the observed temperature (red line) is capable of accurately tracking the hotspot under transient and steady state conditions. The lower plots report the estimation error, which remains in the order of $\pm 5°$ C even during severe thermal transients.

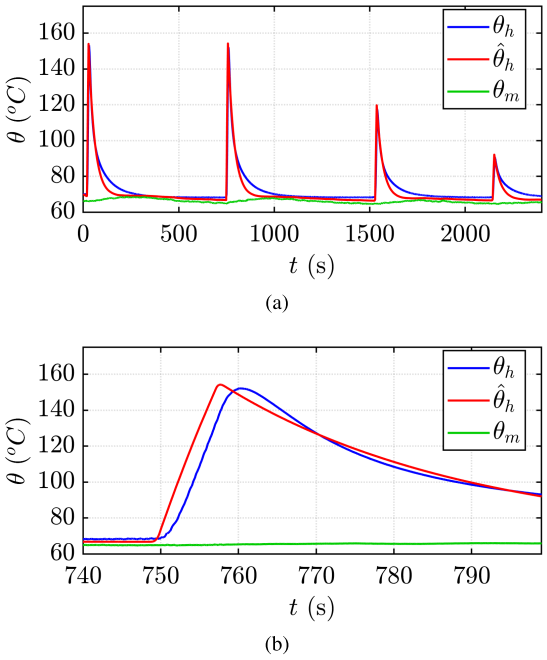

FIGURE 13. Vehicle test: a) Experimentally measured temperature prediction under sharp load steps at maximum speed. Blue and red: measured and estimated hotspot temperature; green: accessible measurement point. b) Zoom of the second load step.

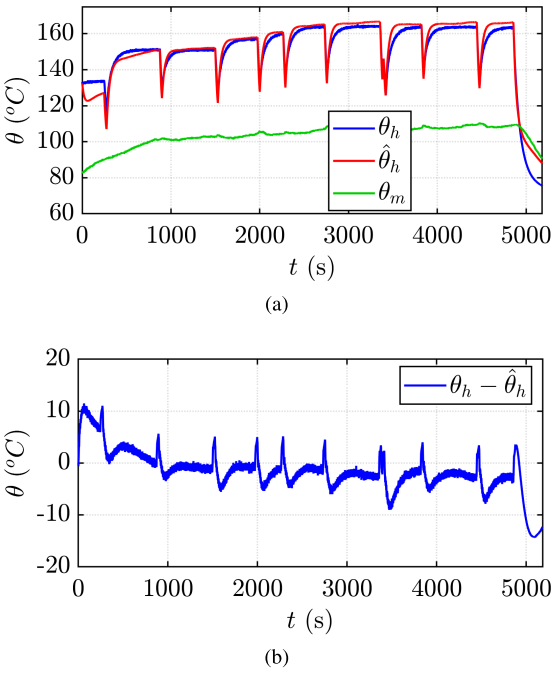

FIGURE 14. Vehicle test: experimentally measured temperature prediction under real driving conditions. a) Blue and red: measured and estimated hotspot temperature; green: accessible measurement point. b) Temperature estimation error.

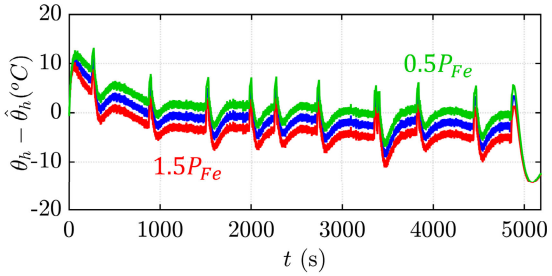

FIGURE 15. Experimental: sensitivity of temperature estimation error under real driving conditions and uncertain $\hat{P}_{Fe}$. Blue: accurate $\hat{P}_{Fe}$; red: $\hat{P}_{Fe}$ overestimated by 20%; green: $\hat{P}_{Fe}$ underestimated by 20%.

B. SENSITIVITY ANALYSIS ON $\hat{P}_j$ ESTIMATION

The Joule losses are affected by the stator resistance variation with its temperature and excitation frequency. Therefore, the estimated $\hat{P}_j$ might be inaccurate, affecting the hotspot temperature observer. To cover this aspect, a sensitivity analysis was conducted in experiments based on the load cycle of Fig. 11 assuming a $\pm 20\%$ error artificially imposed in the $\hat{P}_j$ determination. Fig. 12 reports the corresponding errors in θ_h estimation. Despite the relevant inaccuracy of the input losses, which is above the realistic scenario in automotive, the temperature estimation error remains acceptable, compatible with the specifications imposed by the carmaker.

C. LOAD STEPS AT MAX SPEED

The dynamic accuracy of the proposed hotspot temperature observer was experimentally tested on the vehicle bench imposing sharp torque transients at maximum shaft speed. The test started at steady-state thermal conditions, with the motor temperature determined by the coolant. A series of load steps were commanded to the MUT, maintained for a few seconds, and then released. Sufficient idle time was kept between consecutive load steps to restore the steady-state thermal distribution. Four torque steps of decreasing amplitude were commanded, starting from overload down to partial load. The results, reported in Fig. 13a, demonstrate the capability of the proposed observer to track the hotspot temperature even under such severe thermal transients.

A zoom of the second load step is given in Fig. 13b. As can be noted, the hotspot temperature sharply rises of ≈90° C in only 8 s. Even under such extreme thermal transient, the observed $\hat{\theta}_h$ correctly estimates the hotspot peak, with a limited time delay. The error between the measured and observed peaks of the hotspot temperature in the four load steps was 0.81° C, 2.13° C, 2.31° C, and 1.95° C respectively.

Notably, these transients are extremely fast with respect to the dynamic of the measured temperature (green line), which remains almost constant despite θ_h varying by ≈90° C. Therefore, temperature monitoring based on the measured θ_m is unreliable, and it would easily lead to premature failure of the winding. This confirms the necessity of a hotspot estimator for this high-performance drive.

D. DRIVING CONDITIONS

The proposed hotspot temperature observer was further validated in the vehicle test bench emulating a real driving cycle. The MUT was torque controlled, with the speed

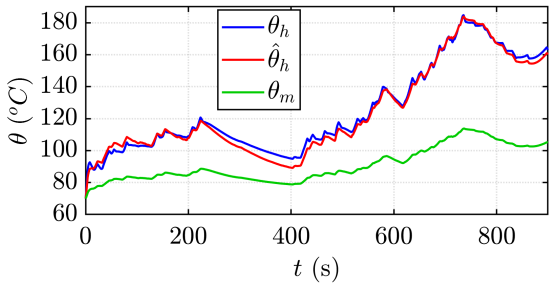

FIGURE 16. Simulation test on a second traction motor of different size under emulated driving conditions. Blue and red: measured and estimated hotspot temperature; green: accessible measurement point.

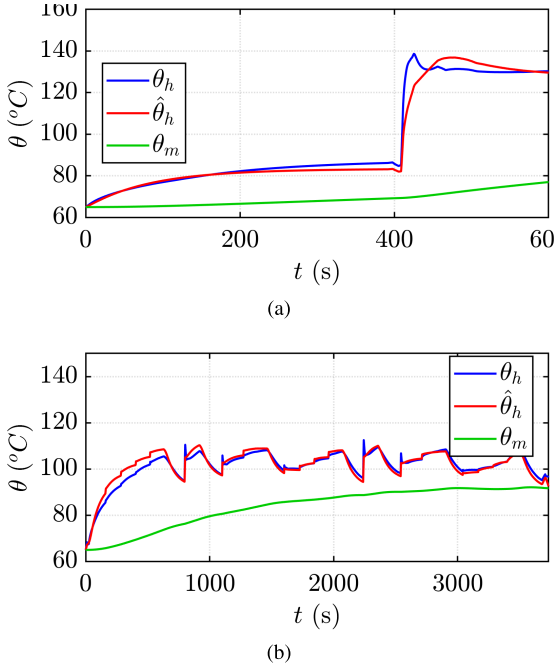

FIGURE 17. Experimental tests on a second traction motor of different size under different driving cycles. Blue and red: measured and estimated hotspot temperature; green: accessible measurement point.

imposed by the bench. The details of the driving cycle are covered by industrial property and cannot be disclosed here. Still, the adopted cycle is made of a sequence of sharp torque variations and accelerations, again covering both partial load and transient overload conditions. The results, reported in Fig. 14, confirm a h otspot temperature significantly higher than the measured one, and varying with a remarkably faster dynamic. Also in this case, the observer is capable of accurately tracking the hotspot, with an error bounded below ±5° C in steady-state and below ±10° C during sharp transients.

E. SENSITIVITY ANALYSIS ON $\hat{P}_{Fe}$ ESTIMATION

Among all the loss terms, iron losses are the most complicated to measure, so a large inaccuracy can be expected in their estimation. For this reason, a further sensitivity analysis was conducted to quantify the effect of an inaccurate $\hat{P}_{Fe}$ estimation on the observed hotspot temperature. In the tests shown in Figs. 13 and 14, the iron losses were estimated using LUTs provided by the carmaker, which were experimentally calibrated to reflect the variation of P_{Fe} with the motor's operating point. These LUTs serve as the reference for the iron loss estimation.

The data collected from the thermal cycle in Fig. 14 were analyzed again, i.e. considering the same load cycle and test conditions, but running the hotspot temperature observer with three different calibrations. The corresponding errors in the temperature prediction are reported in Fig. 15, where the blue line refers to reference $\hat{P}_{Fe}$ (same as Fig. 14) and the green and red curves to ±50% error in iron loss computation. Even under such a large error in the losses, the accuracy of the hotspot temperature tracking is almost insensitive, maintaining a similar estimation error.

F. VALIDATION ON A SECOND TRACTION MOTOR

To demonstrate the scalability of the proposed approach, the hotspot temperature observer was tested both in simulation and experiments on a second motor prototype with a significantly larger rated power in the order of 350 kW. This second machine was characterized using the STTT and SS tests, allowing the calibration of the hotspot temperature observer according to the procedure outlined in Section IV-C. An example of a simulated load cycle is shown in Fig. 16, where the machine undergoes sharp speed and load transients. As illustrated, the hotspot temperature for this second machine is substantially higher than the measurable θ_m and exhibits faster dynamics. Notably, the designed observer successfully tracks the hotspot temperature for this second machine as well, with a transient error bounded within ±5° C.

Two experimental tests are reported in Fig. 17. The first test (Fig. 17.a) consists of two speed and torque transients, while the second (Fig. 17.b) is a complex load cycle. The corresponding torque and speed profile could not be disclosed for confidentiality issues. Also in these cases, the hotspot temperature estimation error is minor, assessing the reliability of the proposed method.

VI. CONCLUSION

This work proposed an effective observer for real-time monitoring of the hotspot winding temperature of a highly-loaded electric motor for traction application. The temperature observer uses an advanced LPTN, calibrated with dedicated experimental commissioning tests. The observer enables the full exploitation of the machine even during sharp transient overload conditions. The LPTN has 7 parameters to be calibrated: 3 thermal capacitances and 4 thermal resistances. The paper describes their calibration including experimental tests and post-processing computation. The hotspot observer is validated both against simulated and experimental data referring to vehicle tests under various drive cycle conditions, showing good accuracy even under erroneous Joule or iron loss estimation. Moreover, the discrete-time solution

of the observer is provided, permitting a rapid real-time implementation with low computational effort.

ACKNOWLEDGMENT

The research was supported by the Power Electronics Innovation Center (PEIC) of Politecnico di Torino.

REFERENCES

[1] S. Ramarathnam, A. K. Mohammed, B. Bilgin, A. Sathyan, H. Dadkhah, and A. Emadi, "A review of structural and thermal analysis of traction motors," *IEEE Trans. Transport. Electrific.*, vol. 1, no. 3, pp. 255–265, Oct. 2015.

[2] P.-O. Gronwald and T. A. Kern, "Traction motor cooling systems: A literature review and comparative study," *IEEE Trans. Transport. Electrific.*, vol. 7, no. 4, pp. 2892–2913, Dec. 2021.

[3] A. Tikadar, D. Johnston, N. Kumar, Y. Joshi, and S. Kumar, "Comparison of electro-thermal performance of advanced cooling techniques for electric vehicle motors," *Appl. Thermal Eng.*, vol. 183, Jan. 2021, Art. no. 116182.

[4] D. Liang, Z. Q. Zhu, B. Shao, J. Feng, S. Guo, Y. Li, and A. Zhao, "Tracking of winding and magnet hotspots in SPMSMs based on synergized lumped-parameter and sub-domain thermal models," *IEEE Trans. Energy Convers.*, vol. 37, no. 3, pp. 2147–2161, Sep. 2022.

[5] R. Leuzzi, P. Cagnetta, S. Ferrari, P. Pescetto, G. Pellegrino, and F. Cupertino, "Transient overload characteristics of PM-assisted synchronous reluctance machines, including sensorless control feasibility," *IEEE Trans. Ind. Appl.*, vol. 55, no. 3, pp. 2637–2648, May 2019.

[6] V. Madonna, A. Walker, P. Giangrande, G. Serra, C. Gerada, and M. Galea, "Improved thermal management and analysis for stator end-windings of electrical machines," *IEEE Trans. Ind. Electron.*, vol. 66, no. 7, pp. 5057–5069, Jul. 2019.

[7] Y. Ji, P. Giangrande, W. Zhao, V. Madonna, H. Zhang, and M. Galea, "Determination of hotspot temperature margin for rectangular wire windings considering insulation thermal degradation and partial discharge," *IEEE Trans. Transport. Electrific.*, vol. 10, no. 1, pp. 2057–2069, Mar. 2023.

[8] T. Dong, X. Zhang, C. Zhu, Y. Lu, and M. Li, "Improved hotspot monitoring method for thermal management system of automotive traction motor," *IET Electr. Power Appl.*, vol. 14, no. 11, pp. 2255–2262, Nov. 2020.

[9] F. Stella, G. Pellegrino, and E. Armando, "Coordinated on-line junction temperature estimation and prognostic of SiC power modules," in *Proc. IEEE Energy Convers. Congr. Expo. (ECCE)*, Sep. 2018, pp. 1907–1913.

[10] D. Reigosa, D. Fernández, M. Martínez, J. M. Guerrero, A. B. Diez, and F. Briz, "Magnet temperature estimation in permanent magnet synchronous machines using the high frequency inductance," *IEEE Trans. Ind. Appl.*, vol. 55, no. 3, pp. 2750–2757, May 2019.

[11] O. Wallscheid, "Thermal monitoring of electric motors: State-of-the-art review and future challenges," *IEEE Open J. Ind. Appl.*, vol. 2, pp. 204–223, 2021.

[12] N. Z. Popov, S. N. Vukosavic, and E. Levi, "Motor temperature monitoring based on impedance estimation at PWM frequencies," *IEEE Trans. Energy Convers.*, vol. 29, no. 1, pp. 215–223, Mar. 2014.

[13] S. Ye and X. Yao, "A modified flux sliding-mode observer for the sensorless control of PMSMs with online stator resistance and inductance estimation," *IEEE Trans. Power Electron.*, vol. 35, no. 8, pp. 8652–8662, Aug. 2020.

[14] C. Kral, A. Haumer, M. Haigis, H. Lang, and H. Kapeller, "Comparison of a CFD analysis and a thermal equivalent circuit model of a TEFC induction machine with measurements," *IEEE Trans. Energy Convers.*, vol. 24, no. 4, pp. 809–818, Dec. 2009.

[15] S. Moon and S. Lee, "High-reliable temperature prediction considering stray load loss for large induction machine," *IEEE Trans. Magn.*, vol. 55, no. 6, pp. 1–5, Jun. 2019.

[16] W. Jiang and T. M. Jahns, "Coupled electromagnetic–thermal analysis of electric machines including transient operation based on finite-element techniques," *IEEE Trans. Ind. Appl.*, vol. 51, no. 2, pp. 1880–1889, Mar. 2015.

[17] C. Sciascera, P. Giangrande, L. Papini, C. Gerada, and M. Galea, "Analytical thermal model for fast stator winding temperature prediction," *IEEE Trans. Ind. Electron.*, vol. 64, no. 8, pp. 6116–6126, Aug. 2017.

[18] L. Jin, Y. Mao, X. Wang, L. Lu, and Z. Wang, "A model-based and data-driven integrated temperature estimation method for PMSM," *IEEE Trans. Power Electron.*, vol. 39, no. 7, pp. 8553–8561, Jul. 2024.

[19] Z. Song, R. Huang, W. Wang, S. Liu, and C. Liu, "An improved dual iterative transient thermal network model for PMSM with natural air cooling," *IEEE Trans. Energy Convers.*, vol. 37, no. 4, pp. 2588–2600, Dec. 2022.

[20] V. Madonna, P. Giangrande, L. Lusuardi, A. Cavallini, C. Gerada, and M. Galea, "Thermal overload and insulation aging of short duty cycle, aerospace motors," *IEEE Trans. Ind. Electron.*, vol. 67, no. 4, pp. 2618–2629, 2020.

[21] T. Huber, W. Peters, and J. Böcker, "A low-order thermal model for monitoring critical temperatures in permanent magnet synchronous motors," in *Proc. 7th IET Int. Conf. Power Electron., Mach. Drives (PEMD)*, Apr. 2014, pp. 1–6.

[22] P. Pescetto, G. Dilevrano, G. Pellegrino, and A. Boglietti, "Real time estimator of winding hotspot temperature for PMSM drives," in *Proc. IEEE Energy Convers. Congr. Expo. (ECCE)*, Nov. 2023, pp. 3822–3828.

[23] Motor Design Ltd. *Motor-CAD Software*. [Online]. Available: https://www.motor-design.com

[24] P. Pescetto, S. Ferrari, G. Pellegrino, E. Carpaneto, and A. Boglietti, "Winding thermal modeling and parameters identification for multithree phase machines based on short-time transient tests," *IEEE Trans. Ind. Appl.*, vol. 56, no. 3, pp. 2472–2480, May 2020.

[25] P. Pescetto, G. Dilevrano, F. Stella, G. Pellegrino, and A. Boglietti, "Enhanced short-time thermal transient model and testing procedure for high power density motors such as in supercar traction," *IEEE Open J. Ind. Appl.*, 2025.

[26] A. Boglietti, E. Carpaneto, M. Cossale, and S. Vaschetto, "Stator-winding thermal models for short-time thermal transients: Definition and validation," *IEEE Trans. Ind. Electron.*, vol. 63, no. 5, pp. 2713–2721, May 2016.

[27] *Rotating Electrical Machines-Equivalent Loading and Super-Position Techniques-Indirect Testing to Determinate Temperature Rise*, Standard IEC60034-29, 2008.

PAOLO PESCETTO (Member, IEEE) received the Ph.D. degree (Hons.) from Politecnico di Torino, Turin, Italy, in 2019. Since 2019, he has been a Researcher and a tenure-track Lecturer with the Energy Department, Politecnico di Torino. He is currently an Assistant Professor with Politecnico di Torino. He is a member of the Power Electronics Innovation Center (PEIC), Politecnico di Torino. In 2014, he was an Erasmus Student with the Norwegian University of Science and Technology, Trondheim, Norway. He has authored or co-authored more than 50 scientific works, with more than 15 IEEE journal articles and five patents. His main research interests include synchronous motor drives, sensorless control, self-commissioning techniques, thermal models, and integrated battery chargers for EVs. He received five IEEE paper awards and two IEEE Ph.D. thesis awards. Since 2022, he has been the Vice Chair of the IEEE IA/IE/PEL North Italy Joint Chapter. He has been an Associate Editor of IEEE TRANSACTIONS ON TRANSPORTATION ELECTRIFICATION, since 2024.

GAETANO DILEVRANO received the M.Sc. and Ph.D. degrees in electrical engineering from Politecnico di Torino, Turin, Italy, in 2020 and 2024, respectively. He has been a Visitor with McMaster University, Hamilton, ON, Canada. He works in an international aerospace company as an electric system and a motor designer with a focus on electric aircraft. His research interests include the design and test procedures of electric motors and drives for electric and hybrid vehicle powertrains with emphasis on innovative electric machines, integration of machine and power converter, and advanced test methodologies.

GIANMARIO PELLEGRINO (Fellow, IEEE) is currently a Professor of power converters, electrical machines, and drives with Politecnico di Torino, Turin, Italy. He has been a Visiting Fellow with Aalborg University, Denmark, the University of Nottingham, U.K., and the University of Wisconsin–Madison, USA. He is the Adjunct Vice Rector of technology transfer with Politecnico di Torino. He initiated and led the development of the open-source platform SyR-e for the design of electrical motors and drives, which is continually enhanced and validated through industry collaborations and is widely adopted worldwide. He has co-authored more than 65 IEEE journal articles and holds nine patents. He is a Founding Member of the Power Electronics Interdepartmental Center (PEIC), Politecnico di Torino, and serves on the Advisory Board of PCIM Europe. He was a recipient of the 8th Grand Nagamori Award. He has received nine best paper awards. He is an Associate Editor of IEEE TRANSACTIONS ON INDUSTRY APPLICATIONS.

ALDO BOGLIETTI (Fellow, IEEE) was born in Rome, Italy, in 1957. He received the Laurea degree in electrical engineering from Politecnico di Torino, Turin, Italy, in 1981. In 1984, he was a Researcher in electrical machines with the Department of Electrical Engineering, Politecnico di Torino. In 1992, he was an Associate Professor of electrical machines and has been a Full Professor with Politecnico di Torino, since November 2000. From 2003 to 2011, he was the Head of the Electrical Engineering Department, Politecnico of Torino. He is the author of more than 200 articles in the field of energetic problems in electrical machines and drives, high-efficiency industrial motor, magnetic material and their applications in electrical machines, electrical machine and drives models, and thermal problems in electrical machines. In 2020, he received the ICEM International Conference on Electrical Machine Arthur Ellison Outstanding Achievement Award. He was a recipient of the Nikola Tesla Award 2024. He is the Past Chair of the Electrical Machine Committee of the IEEE Industry Application Society and the Past Chair of the Electrical Machine Technical Committee of the IEEE Industrial Electronic Society.